

Self-supervised Co-learning of Uncurated Images and Reports Enables Oversight AI in Radiology

Sangjoon Park¹, Eun Sun Lee^{†,2}, Kyung Sook Shin³, Jeong Eun Lee^{†,3}, and Jong Chul Ye^{†,4}

¹Department of Bio and Brain Engineering, KAIST, Daejeon, Korea

²Chung-Ang University Hospital, Seoul, Korea

³Department of Radiology, Chungnam National University Hospital, Chungnam National University College of Medicine, Daejeon, Korea

⁴Kim Jaechul Graduate School of AI, KAIST, Daejeon, Korea

[†]Co-corresponding authors.

[‡]Correspondence should be addressed to J.C.Y. (jong.ye@kaist.ac.kr)

Abstract

Oversight AI is an emerging concept in radiology where the AI forms a symbiosis with radiologists by continuously supporting radiologists in their decision-making. Recent advances in vision-language pre-training sheds a light on the long-standing problems of the oversight AI by the understanding of both visual and textual concepts and their semantic correspondences. However, there have been limited successes in the application of vision-language pre-training in the medical domain, as the current vision-language models and learning strategies for photographic images and captions are not optimal to process the medical data that are usually insufficient in the amount and the diversity. To address this, here we present medical X-VL, a self-supervised model tailored for efficient vision-language pre-training that exploits cross attention in the radiological images and reports' common feature space in a symmetric manner. We experimentally demonstrate that the pre-trained medical X-VL model outperforms the current state-of-the-art models in various vision-language tasks in medical domains. We finally demonstrate practical clinical usages of our oversight AI for monitoring human errors and in the diagnosis of newly emerging diseases, which suggests the potential of an oversight AI model for widespread applicability in different medical applications.

Deep learning has witnessed dramatic advances in vision and language models in recent years, coming closer to human-level intelligence in the fields including the medical domain. However, the successes have been confined within each modality, unlike the human perception being able to be shared between the vision and language concepts. Building a model that can correlate visual and language concepts has been a long-standing topic of research in the field of artificial intelligence (AI)¹. Recently, the vision-language pre-training (VLP), a paradigm of training on a large corpus of image-text pairs aiming to learn shared concepts between images and texts, has attained astounding performance in downstream tasks such as image-text retrieval, vision question answering (VQA), visual grounding, etc., which require both visual and language understanding. As such, VLP has changed the landscape of multi-modal vision-language research, yielding a great number of studies in the past few years²⁻⁸.

The rapid advances of VLP have been indebted to the introduction of vision transformer (ViT)⁹, which processes the images as a set of small patches similar to those of several words for a sentence with the transformer model for natural language processing¹⁰. Thanks to the intrinsic similarities between the ways of processing images and sentences through the self-attention mechanism of the transformer, direct attention between the image patches and words are possible, facilitating more straightforward cross-attention between modalities. Recent works have demonstrated that the transformer-based vision-language models trained with the web-scale image and text data pairs have the generic capability for multiple downstream vision-language tasks^{2,11-14}. Compared with individual models specialized for each task and modality, the vision-language models trained with massive data exhibit superior performances along with the amortization of training cost, enabling to push the limit of model capacity for both domains to reach human-level performances.

In medical fields, rather than completely replacing clinicians' decision-making tasks, there is also an increasing need for oversight AIs to work with clinicians to correct rare but critical errors in their clinical decision-making. In particular, the decision of radiologists usually comes in the form of medical reports so

that visual language models that can understand both the medical images and the reports are an essential step toward the wide acceptance of an oversight AI.

Furthermore, uncurated medical data such as radiograph images and report pairs are already abundant in hospitals, but the absence of manual annotation to discrete labels for traditional supervised learning impedes the utilization of those uncurated image and text pairs to build a robust model. Therefore, making the model directly learn from the uncurated image-report pairs will greatly increase the usability of data, thereby enabling the development of a robust model that can efficiently adapt to various downstream tasks. Nevertheless, there exist only a few studies on the vision-language pre-training in the medical domain^{15,16}, where the pairs of image and sentence are frequently used in the form of radiographs, pathology slides, and corresponding reports.

However, directly adapting the vision-language model in computer vision to the medical domain may result in suboptimal performance due to the different characteristics between the two domains. Compared with the photographic images and captions where billion-scale image-text pairs can be utilized with web crawling^{2,11}, the amount of image-text pairs for medical images is often not sufficient to enable learning a firm relation between visual semantics and textual concept. Furthermore, the diversities between the different images and reports are often more subtle in medical domains than in photographic images (**Supplementary Fig. 1a,b**). For radiographs as an example, the standardized imaging protocols make them consistent in anatomical patterns, and the abnormal findings in radiographs are usually subtly different in appearance¹⁹. Likewise, medical reports usually take the confined words and the sentence structures for a better workflow, producing the structured patterns of words in a sentence except for some keywords to describe the key findings. The relative importance and the uniqueness of the words in a medical report differ more, and those words should be more exact than a caption for a photographic image. For example, given the caption "*The boys are playing on the ground*", the word "*boy*" can be substituted with "*children*" or "*kids*", while not altering the meaning. On the other hand, given the medical report "*No pneumonia or pneumothorax is observed*", the keywords "*pneumonia*" or "*pneumothorax*", which represent the key concepts of the report, are unique and hard to be substituted¹⁶. Therefore, the capability to discriminate those subtle differences and uniqueness is required for the VLP model tailored to the medical domain.

By taking into consideration of the intrinsic properties of images and reports of the medical domain, here we present a model dubbed *Medical Domain X-attention Vision-Language model (Medical X-VL)*, leveraging the key components to be tailored for the medical data. Our medical X-VL employs the cross-attention between image and text by using a fusion encoder that alternatively processes both image-to-text and text-to-image fusions with X-shaped cross attention. We have experimentally demonstrated that the key components of the medical X-VL model are indispensable to attain optimal performance, and also shown that the medical X-VL model outperforms the other state-of-the-art vision-language pre-trained models as well as the versatility to adapt to the wide range of downstream tasks and data in the medical domain (**Fig. 1a**). In particular, we also investigated the clinical feasibility of an oversight AI for various human-caused errors that can be catastrophic and even life-threatening, as well as in the application for emerging diseases in a severely limited data situation. In addition to the quantitative measures, we performed qualitative analysis on the medical X-VL model by visualizing the cross-attention between images and words, providing a transparent interpretation of the model's behavior. Finally, we extended our model to real clinical data of another domain - abdominal radiograph - to demonstrate the wide applicability of the proposed model.

Results

Overview of the proposed model. For vision-language pre-training, most contemporary models can be categorized into two architectures: single-stream and dual-stream architectures²⁰. The single stream architecture^{5,8,21} refers to the model that concatenates visual and text features from uni-modal encoders and processes them with a single multi-modal transformer encoder equipped with self-attention. It is parameter efficient, but is often not pertinent for the joint vision-language understanding tasks like VQA, owing to the missing components to learn fusing visual and text representation. On the other hand, for the dual stream models^{3,12}, the visual and text representations are not concatenated but separately fed into the multi-modal transformer layers. In addition to the intra-modal self-attention, cross-modal attention is used to enable explicit multi-modal interaction to achieve a higher performance as well as joint visual-language understanding. In our

work, the model was developed based on the dual stream architecture, as we aim to develop a versatile model that can adapt to multiple downstream tasks requiring joint vision-language understanding. More detailed descriptions of the differences between the two approaches are provided in **Supplementary Fig. 2a, b**.

Fig. 1b illustrates the overall architecture and the learning objectives of the proposed medical X-VL model. Like the vision-language models based on the cross-attention^{3,22}, it deploys the cross-attention between image and text for vision-language understanding. However, different from the existing models, it uses an alternating fusion encoder that alternatively processes both image-to-text and text-to-image fusions with X-shaped cross-attention. The contrastive learning between image and text, which aims to increase the similarity of image and text features of the same semantic meaning after the uni-modal encoders, enforces the vision and text encoders to embed the image and text features into the same embedding spaces (**Fig. 1c**). This enables the modality agnostic learning, which makes the model have a better understanding of the relationship between the modalities through more efficient data utilization by alternately using the given image-text pair as key/value and query (**Fig. 3d,e**). When not leveraging the contrastive learning to align the image and text features, the model cannot be trained at all as confirmed in **Supplementary Table 1**. Furthermore, since both the fused image features and text features are obtained from the two alternating pathways, the downstream tasks requiring either the fused image or text representation can all be performed in addition to the self-ensemble of both pathways to improve performance (**Fig. 3f**). When ablating either the parameter sharing of fusion encoder by using two separate fusion encoders for image-to-text and text-to-image pathways or self-ensemble of both pathways, the model performances were sub-optimal, as shown in the ablation study (**Supplementary Table 1**).

To learn the correlation between visual semantics and text concepts, the commonly adopted learning objectives include contrastive learning, image-text matching (ITM), and masked language modeling (MLM). Along with these objectives, we utilized masked image modeling (MIM) which serves a similar purpose to MLM that enables the model to learn the intra-modal knowledge by having it complete the imperfect sample. As the MLM and MIM are done with fused text and image features in our model, these can be regarded as image-aided text completion and text-aided image completion tasks, respectively, again enforcing the joint understanding of vision and language concepts. As suggested in **Supplementary Table 1**, the absence of any objective significantly drops the performance, suggesting the distinct roles of each component for model performance. For a detailed description of the model architecture and learning objectives, refer to the Method section.

To strengthen the discrimination ability of the model for subtle differences between data, which is required in the medical domain, we have made use of several additional components: momentum distillation, hard negative mining, and medical keyword weighting. Momentum distillation^{3,23} is a kind of knowledge distillation, a learning method of training the student network under the guidance of the pre-built teacher network that is slowly updated by the student. The teacher-student distillation enables the model to learn the underlying knowledge between the discrete label, under the continuity assumption and clustering assumption²⁴. This is suitable for the medical domain where the similarity between data is high, and therefore the negative samples should be treated differently according to their similarity to the positive pair for better discrimination ability. Secondly, we employed hard negative mining²⁵, a learning strategy that samples "difficult" negative samples with high probability, to enforce the model to attend more to and learn more from the fine-grained details of the samples. Finally, the medical keyword weighting strategy is adopted to assign a higher probability of masking for medical terms during the MLM to account for the different importance of each word in the medical reports. Specifically, we masked a word included in the Medical Subject Headings (MeSH) terms²⁶ with higher probability, such as "*Lung*" or "*Pneumonia*", as it contains key semantic meaning in reports. By having the model predict those MeSH terms more frequently than others, it can get a better understanding of important semantics within images and reports. As provided in **Supplemental Table 1**, ablating any of these components leads to suboptimal performances.

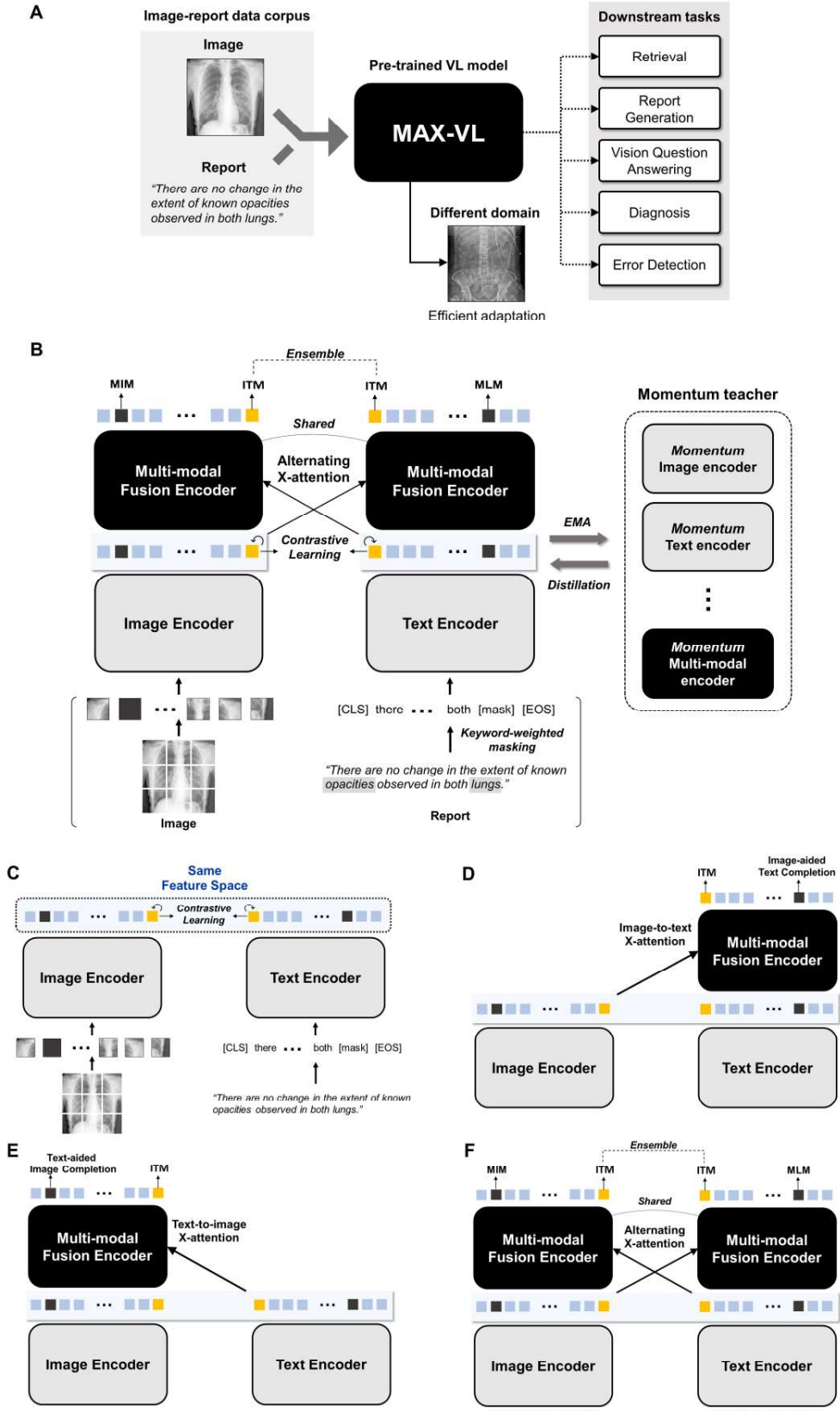


Fig. 1 | (A) The proposed medical X-VL model is pre-trained with an uncurated image-report corpus, and can be utilized for a variety of downstream medical vision and language tasks, and allows the

efficient adaptation to medical data on a different domain. (B) The overview of the model architecture and the learning objectives of the medical X-VL model. (C) Contrastive learning enforces the image and text embeddings to be aligned in the same embedding space. A single multi-modal fusion encoder alternately performs the (D) image-to-text and (E) text-to-image fusions with the X-shaped cross-attention, to learn efficiently from a given image-text pair via image-aided text completion and text-aided image completion. (F) For image-text matching (ITM), the ensemble of both fusion paths can be utilized for better performance. MIM, masked image modeling; ITM, image-text-matching; MLM, masked language modeling; EMA, exponential moving average.

Performances of the proposed model on downstream tasks. Next, we compared the medical X-VL with the existing vision-language models by assessing the model performances for various downstream tasks. For the retrieval and report generation, we used an open-sourced CXR dataset (MIMIC-CXR¹⁸) containing 91,685 image-report pairs. Since we used ITM loss as one of the learning objectives, the zero-shot retrieval was possible with the pre-trained medical X-VL (**Supplementary Fig. 3a**). For report generation, the pre-trained model was fine-tuned with an autoregressive language modeling objective instead of MLM, along with other learning objectives. In detail, the model was trained to predict the next words given the previous sequence of words for the sentence by employing the casual mask to enforce autoregressive generation during the training (**Supplementary Fig. 3b**). For inference, the [CLS] token denoting the start of the sentence is given to the model, and the word next to this [CLS] token is predicted. The predicted word is then appended to the input sequence, and this step repeats until the [SEP] token, denoting the end of the sentence, is generated. Furthermore, to scrutinize the model’s ability to process a challenging task requiring joint vision-language understanding, we experimented on the VQA task with the VQA-RAD dataset²⁷ containing 3,515 pairs of question-answer on 315 images. We fine-tuned the pre-trained medical X-VL model for VQA by deeming the answering task as answer generation³, instead of multi-answer classification (**Supplementary Fig. 3c**)^{5,28}.

Table 1 | Comparison of zero-shot retrieval performances of medical X-VL with other vision-language models.

Method	Image-to-report			Report-to-image		
	R@1	R@5	R@10	R@1	R@5	R@10
w/o VLP	29.4 (12.5)	67.3 (8.2)	86.0 (0.4)	28.8 (14.3)	67.4 (11.6)	86.0 (0.2)
MedViLL ^{15*}	-	78.4	-	-	80.0	-
ALBEF ³	54.2 (1.2)	86.1 (0.7)	93.8 (0.3)	55.5 (0.7)	87.0 (0.3)	92.8 (0.3)
TCL ²²	52.6 (1.2)	84.8 (0.5)	91.5 (0.4)	53.7 (1.1)	85.2 (0.1)	90.8 (0.1)
CoCa ¹²	24.8 (0.4)	59.1 (1.1)	75.6 (1.3)	20.9 (1.0)	54.8 (1.5)	72.3 (1.4)
Proposed	61.3 (1.4)	89.8 (0.2)	95.5 (0.2)	63.2 (0.2)	90.5 (0.3)	95.0 (0.2)

All experiments are performed with three different random seeds, and the means (standard deviations) are provided. * Results from the paper.

Table 1 provides the comparison of retrieval performances between the medical X-VL and other vision-language models. The medical X-VL substantially outperformed the current state-of-the-art medical vision-language model as well as the models for photographic images and texts. In image-to-text retrieval, the model correctly matched the ground truth report corresponding to the given image and retrieved the other image with a similar semantic meaning the second. A report with totally different findings is considered the worst matching one (**Supplementary Fig. 4a**). In text-to-image retrieval, the model correctly retrieved the image corresponding to the given report, and the second-best matching image retrieved by the model also shows almost the same findings (e.g. hyperinflation of the lung with no clear abnormality). On the contrary, the worst matching image considered by the model shows completely different findings (e.g. multiple opacities more severe for the left lower lobe than the right) (**Supplementary Fig. 4b**).

For report generation, the medical X-VL provided overall better performances, both in terms of the evaluation metrics for the text generation in NLP (BLEU-n³¹, ROUGE-L³², METEOR³³, and CIDEr³⁴) and the

clinical accuracy of generated report assessed with CheXpert labeler ³⁵ (**Table 2**). Given the chest radiograph, the model successfully mentioned important semantics (colored text), albeit different in detailed expressions (**Supplementary Fig. 5a**). In addition, it can identify the inadequacy of the image quality due to the problem of patient position during image acquisition (**Supplementary Fig. 5b**).

For VQA, the medical X-VL model outperformed all other models not only for the question specific to chest radiographs but also for the questions regarding all imaging modalities. However, the medical X-VL model showed more prominent superiority in performance for the questions specific to the chest radiographs, which is reasonable that the vision-language pretraining was performed exclusively for the chest radiographs and therefore the benefit from genuine vision-language pretraining should be prominent for this modality while other methods showed similar performances for all questions and the chest radiographs specific questions. In addition, the superiority of the performances was more prominent for the open-ended cases that can be considered to be more challenging than the close-ended ones, probably due to our implementation of VQA as an answer generation problem (**Table 3**). As shown in the exemplified image-question-answer pairs, the model correctly answered the multiple pathologies of the given image for the open-ended question as well as the close-ended question, which requires the understanding of the lesion location and right-left orientation and their relationship (**Supplementary Fig. 6a,b**).

Table 2 | Comparison of report generation performances of medical X-VL with other vision-language models.

Method	Clinical evaluation						
	BLEU-4	METEOR	ROUGE-L	CIDEr	Accuracy	Precision	Recall
w/o VLP	0.041 (0.002)	0.082 (0.009)	0.175 (0.009)	0.046 (0.001)	67.9 (0.3)	54.1 (0.2)	38.3 (6.5)
MedViLL ¹⁵	0.023 (0.001)	0.109 (0.002)	0.136 (0.001)	0.009 (0.002)	71.1 (0.5)	58.0 (0.7)	53.3 (0.9)
ALBEF ³	0.058 (0.006)	0.112 (0.001)	0.197 (0.001)	0.082 (0.005)	73.7 (0.4)	62.3 (0.5)	57.4 (0.8)
TCL ²²	0.056 (0.002)	0.112 (0.001)	0.196 (0.001)	0.079 (0.007)	73.3 (0.3)	61.7 (0.3)	57.1 (0.9)
CoCa ¹²	0.040 (0.002)	0.092 (0.001)	0.169 (0.003)	0.052 (0.004)	71.5 (0.3)	58.8 (0.1)	54.5 (2.1)
Proposed	0.060 (0.003)	0.114 (0.001)	0.200 (0.001)	0.086 (0.004)	73.5 (0.3)	62.0 (0.5)	57.5 (0.4)

All experiments are performed with three different random seeds, and the means (standard deviations) are provided.

Table 3 | Comparison of VQA performances of medical X-VL with other vision-language models.

Methods	All		Chest	
	Open	Closed	Open	Closed
No VLP	36.0 (6.3)	65.5 (2.6)	0.0 (0.0)	51.7 (0.0)
MedViLL ^{15*}	59.7	78.2	60.8	78.3
MEVF ^{29*}	40.7	74.1	-	-
PubMedCLIP-MEVF ^{30*}	48.6	78.1	-	-
PubMedCLIP-QCR ^{30*}	60.1	80.0	-	-
ALBEF ³	60.0 (0.6)	78.2 (1.2)	60.9 (1.0)	80.7 (4.1)
TCL ²²	59.0 (4.0)	79.0 (1.3)	62.1 (3.4)	78.7 (1.0)
Proposed	62.0 (0.6)	79.7 (1.2)	64.4 (1.0)	83.9 (1.3)

All experiments are performed with three different random seeds, and the means (standard deviations) are provided. * Results from the paper.

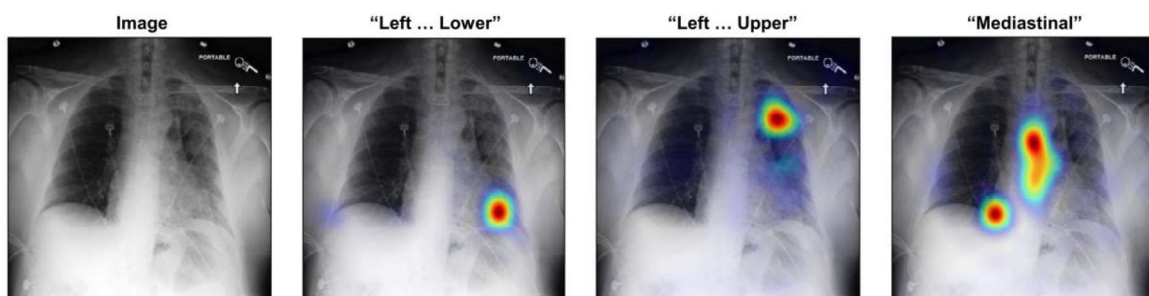
Verification of image-text binding via qualitative analysis of cross-attention. To provide a transparent interpretation of the model’s behavior, we performed qualitative analysis using the Grad-CAM³⁶ visualization for the fusion encoder’s cross-attention, as suggested in the ALBEF³, as depicted in the exemplified cases of **Fig. 2a,b**. Without any supervision for the region-word correlations, the medical X-VL model correctly focuses on the regions related to each word, demonstrating its ability to understand the relationship between

the semantics of the image and the textual concept. Notably, the model not only grounds the important clinical findings (“Congestion”, “Pacemaker”) but also understands the location (“Mediastinal”, “Cardiac”) and the relationships (“Left ... Lower”, “Left ... Upper”).

Oversight AI for human error detection. In clinics, several human errors like right-left orientation confusion or patient-report misregistration rarely occur but may lead to fetal results. As our medical X-VL has a comprehensive understanding of visual semantics and textual concepts, we assessed whether it can detect and correct human errors in sentences. For the detection of an error, we hypothesized that the image-report matching score may be altered if the error occurs, as the resulting erroneous report may not be matched to the given image. We simulated human errors by generating errors, mimicking the critical human-made errors in clinics.

First, the word “right” was changed to “left” and vice versa with a probability of 5%, to emulate the right-left orientation confusion, and we evaluated whether the model can detect and correct the wrong word automatically. As shown in Fig. 5A, the pre-trained medical X-VL can detect the right-left orientation error with the AUC of 0.759 ± 0.067 , without any supervision. In addition, thanks to the image-aided MLM in pre-training objectives, it can correct erroneous reports by substituting wrong words (red text) into correct ones (green text) referring to the image, when masking each word within a sentence one by one and predicting it. Interestingly, the model sometimes substituted other words (“enlargement” to “widening”) as shown in the green text of Fig. 3a, which does not significantly alter the overall meaning of the sentence.

A Sternotomy wires and mediastinal clips are unchanged. The cardiomeastinal contours are unchanged. There is increased consolidation of the left lower lung as well as in the upper lung. There is no large pleural effusion or pneumothorax. The right lung is clear.



B In comparison with the study of ____, there again is enlarged of the cardiac silhouette in a patient with intact midline sternal wires and pacemaker device in place. Engorged and indistinct pulmonary vessels are consistent with increasing pulmonary venous congestion.

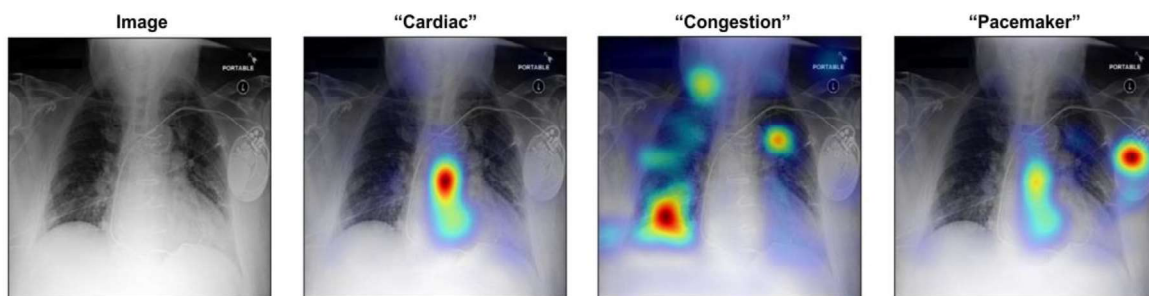


Fig. 2 | (A-B) Exemplified cases of the Grad-CAM visualization of the cross-attention maps corresponding to each word. The medical X-VL model not only grounds the important clinical findings (“Congestion”, “Pacemaker”) but also understands the location (“Mediastinal”, “Cardiac”) and the relationships (“Left ... Lower”, “Left ... Upper”).

Next, given a radiograph image, the original report was substituted with an unmatched report with a probability of 1% to emulate the misregistration error. We evaluate whether the model can detect misregistration and suggest a matching report for the image. As shown in Fig. 3b, the model can accurately

detect the misregistration with an AUC of 0.981 ± 0.025 , and successfully suggested the exactly matching report or those with semantically identical meanings as in the exemplified case.

Utility of vision-language pre-training for emerging disease. Considering that the human reader usually interprets newly encountered findings in an image with already learned language concepts, it is expected that a comprehensive understanding of vision and language will provide more efficient adaptation to downstream tasks like classification, compared with merely learning the semantic features via self-supervised learning.

Therefore, we hypothesized that the vision-language pre-trained model will also exhibit fine-tuned performance superior to the self-supervised model, especially in terms of generalization ability, given the limited data availability. To simulate the data-limited setting, we fine-tuned the visual encoder of medical X-VL and other self-supervised models using a highly limited number of COVID-19 data containing only 181 COVID-19 and 276 non-COVID-19 images (**Supplementary Fig. 3d**). Then, we evaluated the generalization ability of the model to the external validation dataset from three hospitals labeled by board-certified radiologists, containing 660 COVID-19 and 1,117 non-COVID-19 images. For details on the datasets, refer to the Method section.

As shown in **Table 4**, the vision-language pre-trained medical X-VL showed generalization performances superior to those pre-trained with the contemporary self-supervised learning methods as well as the baseline without pre-training, indicating its utility for prompt development of a robust model with an extremely small number of data, given a newly emerging disease (**Supplementary Fig. 7a,b**).

A Right-left orientation confusion

AUC = 0.759 ± 0.067



True: In comparison with the study of ___ the monitoring and support devices are unchanged. there is again substantial **enlargement** of the cardiac silhouette with pulmonary vascular congestion and bilateral pleural effusions more prominent on the **right**.

Wrong: In comparison with the study of ___ the monitoring and support devices are unchanged. there is again substantial enlargement of the cardiac silhouette with pulmonary vascular congestion and bilateral pleural effusions more prominent on the **left**.

Corrected: In comparison with the study of ___ the monitoring and support devices are unchanged. there is again substantial **widening** of the cardiac silhouette with pulmonary vascular congestion and bilateral pleural effusions more prominent on the **right**.

B Patient-report misregistration

AUC = 0.981 ± 0.025



Wrong: The patient remains intubated with the ET tube tip is 7 cm above the carina. The NG tube tip passes below the diaphragm with its tip not clearly seen on the current examination. The right internal jugular line tip is at the level of mid SVC. The patient is in pulmonary edema, moderate, progressed since the prior study, associated bilateral pleural effusions.

Suggestion: Single portable view of the chest. Lower lung volumes seen on the current exam. Patchy region of opacity identified at the left lung base. Elsewhere, the lungs are clear. The cardiomeastinal silhouette is within normal limits. Tortuosity of the descending thoracic aorta is noted.

Fig. 3 | (A) Example for the detection and correction of the right-left orientation error. Notably, other than the wrong words, it also changes another word (“enlargement”) to another (“widening”) without significantly changing the meaning. (B) Example for the detection of the patient-report mismatching error, and the model’s suggestion for the correct matching report. AUC, area under the receiver operating characteristics curve. Experiments are performed with three random seeds and means \pm standard deviations are provided.

Table 4 | Comparison of classification performance for COVID-19 in the highly data-limited setting.

Methods	AUC	Accuracy	Precision	Recall
No pretrain	0.693 (0.121)	37.4 (0.4)	37.4 (0.0)	100.0 (0.0)
SimCLR ³⁷	0.788 (0.092)	77.0 (5.1)	74.9 (13.2)	60.1 (7.7)
DINO ³⁸	0.842 (0.026)	79.3 (2.7)	76.1 (7.9)	65.8 (2.6)
SimMIM ³⁹	0.748 (0.081)	44.6 (6.5)	40.2 (2.8)	99.5 (0.5)
Proposed	0.882 (0.030)	80.5 (5.3)	71.6 (8.1)	80.5 (2.9)

All experiments are performed with three different random seeds, and the means (standard deviations) are provided.

Application to real clinical data in different domain. To investigate the widespread applicability, we extended our work to the domain of abdominal radiographs. A total of 8,201 abdominal radiograph image-text pairs were collected from two hospitals (Chung Ang University Hospital [CAUH] and Chungnam National University Hospital [CNUH]) were used for the vision-language pre-training on abdominal radiographs, and the other 235 images collected from a separated group of patients were utilized as the validation dataset. We initialized the model with pre-trained weights from chest radiographs, as there exist common semantics between the chest and abdominal radiographs albeit different in the field of view. The clinical accuracy of the generated reports was evaluated whether or not the model found out and mentioned the abnormal clinical findings (e.g. ileus, pneumoperitoneum) in the generated report, given an abdominal radiograph.

As provided in **Table 5**, the quality of the report generated by the medical X-VL model was good in terms of both the metrics for generated sentences in NLP and the clinical accuracy. As shown in the examples, the model correctly generated a report describing the pathologic findings as well as the normal condition (**Supplementary Fig. 8a,b**). The performances of the vision-language pre-trained model were significantly better than those without, showing the necessity of the vision-language pre-training for a comprehensive understanding of images and texts regardless of the downstream tasks. The direct training of the model for report generation without the vision-language pre-training was unsuccessful, resulting in non-discriminative repetition of the same report for all images.

Table 5 | Report generation performances of the medical X-VL model for abdominal radiographs

Method	Clinical evaluation						
	BLEU-4	METEOR	ROUGE-L	CIDEr	Accuracy	Precision	Recall
w/o VLP	0.593 (0.002)	0.381 (0.001)	0.746 (0.001)	5.549 (0.001)	76.9 (0.2)	0.0 (0.0)	0.0 (0.0)
Proposed	0.612 (0.004)	0.454 (0.007)	0.787 (0.009)	6.067 (0.040)	90.1 (0.6)	86.9 (4.5)	67.4 (5.2)

All experiments are performed with three different random seeds, and the means (standard deviations) are provided.

Discussion

Recently, deep learning-based AI models have achieved astonishing progress in an increasing range of tasks but their successes have been confined to narrow domains, throwing doubt that something fundamental is still unaccounted for. Although contemporary AI-based CAD models provide excellent detection performances to detect abnormalities within an image, they are mainly designed as independent diagnostic tools which often interfere with common radiological workflow. They also lack the complementary ability to help human readers, such as finding errors in the report describing the image because they are unable to understand the image and text together.

In contrast to the traditional supervised learning in which visual recognition learning is tackled with the manually annotated image-label pair, the uncurated image-text pair is given to the model in the learning

process of vision-language pre-training. The merit of vision-language pre-training in computer vision applications is that the vision-language model can learn rich semantics with the broad coverage of visual concepts from the free-form text instead of discrete labels that provide dense but confined visual concept⁴⁰. By learning the broad visual semantics along with the corresponding textual concepts, the model can easily attain good performances in a variety of downstream tasks, ranging from retrieval to text generation. Nevertheless, there remain unsolved problems such that the image-text pair, albeit offering broad coverage of visual concepts, generally lacks the powerful discriminative ability compared with the dense label for traditional supervised learning. Consequently, billion-scale image-text data, which is extremely difficult to obtain for the medical domain, are usually required to train a robust vision-language model as shown in the study of CLIP¹¹ and ALIGN².

To cope with the problem, we leveraged several methods to maximally exploit the correlated semantics from each data. Given an image-text pair, we utilized the alternating fusion pathways, namely image-to-text and text-to-image fusions, enabling the model to learn once from image-guided text and once from text-guided image understandings. In our approach, this was possible thanks to the contrastive learning between the features after the uni-modal encoder that induces the image and text features to be aligned in the same embedding space before the fusion. Furthermore, the two methods - knowledge distillation, and hard negative mining- were utilized during the training. The knowledge distillation enables the model to learn the hidden knowledge between the positive and negative samples, by not treating all negative samples uniformly but according to their similarities to the positive sample. Hard negative mining, which draws a similar negative sample with a high probability, also enforces the model to learn more about the discrimination between similar data. Combined, these two methods improve the discrimination ability to relatively small variation between the samples in the medical domain. Finally, to account for the importance of the unique medical terms, the medical keyword weighting that applies more weights to the clinically important expressions was utilized during the MLM. With these components, the proposed medical X-VL model could surpass the contemporary medical deep learning model as well as the state-of-the-art vision-language model for photographic images and captions in various downstream tasks.

Thanks to the proposed improvement, we were able to demonstrate the utility of our medical X-VL model in diverse clinical applications. In clinics, critical human-made error, like orientation confusion and misregistration, rarely occurs but can lead to disastrous result. Our medical X-VL model can successfully detect the errors with high accuracy, and even automatically corrects them or retrieves the matching pair without any supervision. In addition, compared with the other contemporary self-supervised learning approaches, the generalization ability of the vision-language pre-trained model was superior, given the extremely data-limited setting. These results suggest that the visual and textual concepts that the model learned through vision-language pre-training can be shared irrespective of disease entities, and can be efficiently utilized for the newly emerging disease like COVID-19 in 2020, especially in the early stage of the outbreak when the data availability matters most.

Our study has several limitations. First, since the form of the medical report for chest radiographs is not standardized, the generated reports are arbitrary and different from the original report in detail, albeit containing semantically similar meanings (Supplementary Fig. S3). This results in relatively low scores for the natural language evaluation metrics, compared with those reported for the photographic images and caption pairs in the previous works^{7,12,41}. Further study is required using the other imaging modalities in which the structured report form is widely adopted. Second, although our method enables vision-language learning with uncurated image-report data stored in each institutional database, the dependency on pre-built image-report paired data can be regarded as a limitation. For photographic images and captions, an automated web crawling algorithm can be used to build a billion-scale data corpus^{2,11}, but this is not feasible for medical images and reports.

Nevertheless, we have demonstrated that our medical X-VL introduced to the medical domain can be effectively applied to the medical domain as an oversight AI. In particular, we investigated the clinically useful applications in a real-world setting, like error detection, correction, and fast adaptation to newly emerging diseases, which may lead to improved clinical practice. Considering the general configuration of image-report pairs in medical imaging modalities other than radiographs, we believe that our method possesses broad applicability in the field of medical imaging.

Methods

Details of model architecture. Our medical alternating cross-attention vision-language (medical X-VL) model follows the general structure of the dual stream cross-attention based vision-language models^{3,12,22,42}, but is different in the use of multi-modal fusion encoder that alternates between the image-to-text and text-to-image cross-attention. This fusion encoder is shared between two pathways, namely image-to-text and text-to-image fusion, enabling more efficient utilization of data pairs. An input image I is encoded to the sequence of patch embeddings $\{p_{cls}, p_1, \dots, p_N\}$ by the image encoder, where p_{cls} denotes the [CLS] token embedding. Likewise, an input text T is transformed to the sequence of word embeddings $\{w_{cls}, w_1, \dots, w_M\}$, where w_{cls} is the [CLS] token that also means the start of the sequence and w_M is the [SEP] token to represent the end of the sentence. With the alternating multi-modal fusion encoder, the patch embeddings fuse with the word embeddings to yield the fused patch embeddings $\{u_{cls}, u_1, \dots, u_N\}$ using the cross-attention, and vice versa for the fused word embeddings $\{v_{cls}, v_1, \dots, v_M\}$, making use of an X-shaped cross attention between the modalities. In our experiment, using separate fusion encoders for each pathway meaningfully dropped the performance, suggesting the benefit of the shared encoder for efficient data utilization (**Supplementary Table 1**).

Details of pre-training objectives. The proposed medical X-VL model is trained with four learning objectives: contrastive learning for cross- and intra-modal alignment, masked language modeling (MLM) for image-guided text completion, masked image modeling (MIM) for text-guided image completion, and image-text matching (ITM).

Contrastive Learning for Cross- and Intra-modal Alignment. Cross-modal contrastive learning aims to align the image and text features in the same embedding space before the fusion, by applying the uni-modal encoders. Specifically, it pulls the positive image-text pair together while pushing the unmatched pair apart. Given the encoded embeddings p_{cls} and w_{cls} of [CLS] tokens of the image I and text T , similarity function $sim(I, T)$ and $sim(T, I)$ can be defined as:

$$sim(I, T) = h_I(p_{cls})^T h_T(w_{cls}), \quad sim(T, I) = h_T(w_{cls})^T h_I(p_{cls}) \quad (1)$$

where h_I and h_T denote linear projectors with normalization layers for image and text features.

Then, the normalized image-to-text and text-to-image similarities of each image-text pair are calculated as:

$$s_{i2t} = \frac{\exp(sim(I, T_m)/\tau)}{\sum_{m=1}^M \exp(sim(I, T_m)/\tau)}, \quad s_{t2i} = \frac{\exp(sim(T, I_n)/\tau)}{\sum_{n=1}^N \exp(sim(T, I_n)/\tau)} \quad (2)$$

where τ denotes the temperature parameter.

Meanwhile, intra-modal contrastive learning aims to teach the model about the semantic differences between positive and negative samples within the modality. Similar to cross-modal contrast learning, the normalized image-to-image and text-to-text similarities can be defined as:

$$s_{i2i} = \frac{\exp(sim(I, I_n)/\tau)}{\sum_{n=1}^N \exp(sim(I, I_n)/\tau)}, \quad s_{t2t} = \frac{\exp(sim(T, T_m)/\tau)}{\sum_{m=1}^M \exp(sim(T, T_m)/\tau)} \quad (3)$$

where τ is the same temperature parameter used in cross-modal contrastive learning.

Consequently, given the one-hot label similarity y , the cross-modal contrastive loss L_{CMC} , intra-modal contrastive loss L_{IMC} , and overall contrastive loss $L_{contrastive}$ can be defined as the cross-entropy

loss H :

$$L_{CMC} = \frac{1}{2} [H(y_{i2t}, s_{i2t}) + H(y_{t2i}, s_{t2i})] \quad (4)$$

$$L_{IMC} = \frac{1}{2} [H(y_{i2i}, s_{i2i}) + H(y_{t2t}, s_{t2t})] \quad (5)$$

$$L_{contrastive} = L_{CMC} + L_{IMC} \quad (6)$$

Inspired by the recent contrastive learning approaches⁴³, we have the image and text queues to store the most recent Q samples from the momentum encoder for each modality. In our experiments, the queue size Q was 49,152.

As the feature similarities can be calculated between image and text with the above objectives, these similarities can also be utilized in hard negative mining for ITM, by sampling the negative pair with high similarity more frequently. Additionally, this learning objective enables the alternating fusion encoder to process both image-to-text and text-to-image fusion, which seems to be unreasonable at first glance as the same key, query, and value weights are shared between different modalities, by aligning the image patch and the word features in the same embedding space. In our experiments, ablating the contrastive learning objective substantially degraded the performance, showing that this aligning process is essential for the learning alternating fusion encoder shared between the modalities (**Supplementary Table 1**).

Masked Language Modeling for Image-guided Text Completion. Masked Language Modeling (MLM) is a commonly adopted learning objective to obtain language understanding to predict the ground truth of the masked word tokens w_{mask} from other unmasked word tokens, with the aid of the corresponding image in our model. In detail, the word tokens are masked out with a probability of 15% and replaced with the [MASK] token with 80%, the random word token with 10%, and the unchanged original token with 10% probabilities⁴⁴. Let the masked text as T^{mask} , the prediction for [MASK] tokens after fusion encoder as $p^{mask}(I, T^{mask})$, and the ground truth for each word token as y_w^{mask} , the MLM loss in our model can be defined with cross-entropy loss H :

$$L_{MLM} = H(y_w^{mask}, p^{mask}(I, T^{mask})) \quad (7)$$

As the predictions for the [MASK] token come from the multi-modal fusion encoder which fuses the image representation into text tokens, our MLM task can be considered as an image-aided masked text token prediction. Consequently, the model comes to understand the joint image-text representation and their relationship.

Masked Image Modeling for Text-guided Image Completion. Similar to MLM, we also employed masked image modeling (MIM) to enable the model to learn the comprehensive image-text joint understanding, performing the task of text-guided masked area completion. Specifically, instead of directly predicting the pixel values of masked image patches, we utilized the distilled online token prediction method proposed in the study of iBOT⁴⁵. Given an image I , image patch tokens $\{x_{cls}, x_1, \dots, x_N\}$ are blockwisely masked with a random mask $M = \{m_1, \dots, m_N\} \in \{0, 1\}^N$ with masking ratio r by substituting image token x with the mask token [MASK], where $m_i = 1$ indicates the masked patch tokens, making a masked image I^{mask} . For the set of masked patch tokens $\mathbf{x}_{masked} \triangleq \{x_i \mid m_i = 1\}$, the model learns to match its prediction of the masked patch token after the fusion encoder $p^{mask}(T, I^{mask})$ similar to the label y_w^{mask} , referring to both the unmasked image area and the corresponding text. Similar to the iBOT that uses the momentum teacher as an online tokenizer instead of the offline discrete tokenizer like BEiT⁴⁶, the labels for masked patch tokens were generated by the momentum teacher parameterized by $\hat{\theta}$. Consequently, the learning objective of the model parameterized by θ can be defined as:

$$L_{MIM} = H\left(\mathbf{y}_p^{mask}, \mathbf{p}^{mask}(T, I^{mask})\right) = \sum_{i=1}^N \mathbf{m}_i \cdot P_{\hat{\theta}}(x_i) \log P_{\theta}(x_i) \quad (8)$$

This can be considered as text-aided image completion, which again enforces the model to learn the mutual relationship between image and text representations.

Image-Text Matching. Image-text matching directly predicts whether a given image-text pair is matched or unmatched. We utilized the fusion embeddings of two [CLS] tokens obtained from the outputs of image-to-text and text-to-image paths of the fusion encoder, as they both imply the joint representation of the image-text pair. Following the fusion embeddings, we appended the binary classifiers to predict the prediction $c^{itm}(I, T)$ for matching each image-text pair. Given y^{itm} as the ground truth label for image-text matching, the ITM loss can be defined with cross-entropy loss H as below:

$$L_{ITM} = H\left(\mathbf{y}^{itm}, \mathbf{c}^{itm}(I, T)\right) \quad (9)$$

We additionally employed hard negative mining for ITM, by drawing the samples with high similarity s_{I2t} and s_{t2I} with high probability when sampling negative pair from the batch for a given image or text³. As the semantically similar negatives can be regarded as hard negatives that only differ in fine-grained details, this allows the model to get better discrimination capability to catch subtle differences, which are especially important for medical imaging where the differences between images are small owing to the standardized acquisition protocol. With this strategy, the model performances were significantly improved with zero computational overhead.

Combined, the overall pre-training objective L of the medical X-VL is:

$$L = L_{contrastive} + L_{MLM} + L_{MIM} + L_{ITM} \quad (10)$$

Momentum Distillation. In contrastive learning, some negative samples may also have a similar context to the positive ones and need to be treated differently from the entirely different negative samples. For example, given a radiograph showing the bibasilar opacifications suggesting the sign of pneumonia, other than the exactly matching description “*There is newly developed bibasilar opacification suggesting newly developed pneumonia*”, a report like “*There exist lung opacities in both lower lobe suggesting the severe pleural effusion*”, albeit describing different etiology for opacification and therefore may be regarded as a negative sample, should be penalized differently compared with an entirely unmatching description “*Both lung fields are clear and there is no remarkable finding*”. This matters more in the medical domain, where the differences between the images and reports are smaller than the photographic images and captions; therefore, overlapping between the images or reports can be substantial. Similarly, for MLM, there may exist other candidates different from the ground truth but have the semantically same meaning like “*No remarkable findings*” and “*No abnormality*”. However, the binary and one-hot coded labels for contrastive learning and MLM penalize all negative samples without considering their correctness.

Therefore, we employed the momentum teachers, which are gradually updated with exponential moving averaging of updated models, and generated pseudo labels for contrastive learning and MLM. During the training, the model is optimized to match the pseudo labels generated from the momentum teacher by minimizing distillation loss L_{dist} as well as the aforementioned overall loss L , with weights λ to balance the contributions of momentum distillation as follows:

$$L_{total} = (1 - \lambda) \cdot L + \lambda \cdot L_{dist} \quad (11)$$

Details for Model for Downstream Tasks. We adapted and assessed the pre-trained VL models for several downstream tasks. **Supplementary Fig. 3** illustrates the modification of the pre-trained medical X-VL model for the specific downstream tasks. For retrieval, we could directly evaluate the zero-shot retrieval performances, since the L_{ITM} was included as a component of pre-training objectives (**Supplementary Fig. 3a**). For report generation, the model was fine-tuned by substituting MLM with the next word prediction, to

allow the auto-regressive generation of reports similar to image captioning (**Supplementary Fig. 3b**). As for the VQA, we deemed VQA as an answer generation instead of multi-answer classification^{5,28}, similar to the approach taken in recent works^{3,22}. We utilized the BERT_{base} model to fuse the image features and question into fused features and used the six-layered transformer decoder to generate the answer in an auto-regressive manner (**Supplementary Fig. 3c**). For classification, we utilized the vision encoder of the medical X-VL model, to compare with the same-sized ViT model trained with the existing self-supervised learning approaches (**Supplementary Fig. 3d**).

Details of datasets. For the vision-language pre-training with chest radiographs, we utilized the MIMIC-CXR dataset¹⁸, an open-sourced database containing 377,110 image and report pairs. Among these images, we only utilized the 91,685 anterior-posterior (AP) view images and followed the train, validation, and test sets division provided by a previous study of MedViLL¹⁵ for the comparison, resulting in 89,395, 759, and 1,531 images for training, validation, and testing, respectively. As the reports of MIMIC-CXR contain several descriptions (e.g. impression, findings, etc.) that are all redundant in content, we selected a longer description for each report, as proposed in a previous work¹⁵. For VQA, we utilized the VQA-RAD dataset²⁷ containing 3,515 question-answer pairs on 315 images, not only for the chest radiographs but also for the other medical imaging modalities. Among those question-answer pairs, 3,064 were used for training and 451 for testing, following the original division by the dataset provider. To investigate the utility of the vision-language pre-trained model on the newly emerging disease with COVID-19 classification, we used 181 chest radiographs of COVID-19 positive cases and 276 chest radiographs of the normal cases from the Brixia⁴⁷ and the NIH datasets⁴⁸, respectively for training, making a limited dataset containing a total of 457 chest radiographs. We evaluated the generalization performance of the trained model on the external validation dataset consisting of 660 COVID-19 and 1,117 chest radiographs collected from three hospitals (Chungnam National University Hospital [CNUH], Kyungpook National University Hospital [KNUH], Yeungnam University Hospital [YNU] labeled by the board-certified radiologists). For the experiments on the abdominal radiograph, the inpatient databases of two hospitals were used. In detail, the 5,776 erect abdominal radiographs from the CAUH and the 2,425 erect abdominal radiographs from the CNUH were collected without curation and integrated to make an entire training dataset containing 8,201 images. For the test set, the data containing 235 erect abdominal radiographs from a different patient group are separately collected, which contains the cases with 181 normal and 54 abnormal findings.

Implementation details. The image data were pre-processed by cutting margin space as proposed in a previous work¹⁵, and underwent Gaussian blurring, normalization, and resized to 224×224 . For the visual encoder, we used the ViT-S/16 model pre-trained on ImageNet and the same visual encoder was used for ALBEF³, TLC²², and CoCa¹². For MedViLL, the CNN-based visual encoder was utilized for the MedViLL as proposed in the original work¹⁵. Similar to the previous vision-language model having cross-attention^{3,22,42}, the first six layers of the uncased BERT_{base} model⁴⁴ were used as the text encoder, while the last six layers of the BERT_{base} were utilized as the fusion encoder. We trained the text tokenizer with the word corpus of the MIMIC-CXR dataset that occurs at least once with a vocabulary size of 30,522, and the maximum length of the report was set to 100. For the vision-language pre-training, an AdamW optimizer with the initial and maximal learning rate of 0.00001 and 0.0001 was used for the 15 epochs including five epochs of the warm-up period, and the batch size was 12. For fine-tuning each task, we used the different hyperparameters according to the tasks, as suggested in **Supplemental Table 2**. For the performance comparison in a highly data-limited setting between the contemporary self-supervised learning methods, the ViT-S/16 models same to the visual encoder are trained with hyperparameters specified in **Supplemental Table 3**. All experiments were performed using Python version 3.8 and Pytorch library version 1.10 on NVIDIA GeForce RTX 3090.

Details of evaluation. For the evaluation of the retrieval performance, we reported the retrieval accuracy at ranks 1, 5, and 10 (R@1, R@5, and R@10). As the rank-based retrieval accuracy can differ according to the size of the test datasets, we randomly divided the test dataset into 100 image-report pairs and calculated the retrieval accuracy similar to the study for comparison¹⁵. This evaluation was performed with 10 different random seeds to obtain reliable results. Unlike the photographic image and caption, there may exist reports that are different in expression but have the semantically same meaning. For example, the reports "No abnormal findings" and "Nothing remarkable." are different in expression, but semantically the same. If the model successfully retrieves either of these reports and if there is nothing remarkable in the radiograph, it should be considered as correct. Therefore, we defined it as a matching pair if they contain exactly the same label classes with CheXpert labeler³⁵, and unmatching pair if not¹⁵. The evaluation of report generation

performance was done in two aspects, the metrics to evaluate generated sentences in NLP like BLEU³¹, METEOR³³, ROUGE-L³², and CIDEr³⁴, and the metrics for clinical accuracy of the generated reports after labeling them with the CheXpert labeler³⁵. To evaluate the clinical accuracy of generated reports for abdominal radiographs, whether or not clinically important findings (e.g. pneumoperitoneum, ileus, etc.) are mentioned in the report generated by the model was assessed by a clinician, referring to both the original report and the image. For VQA, since the model is pre-trained with the chest X-ray dataset, we separately assessed the adaptation capability of the model for all questions regarding the chest radiographs. In addition, following the VQA-RAD paper²⁷, the accuracy of the open-ended and closed-form questions are reported separately. The pre-processing for the answer was performed to unify the answers with the same semantic meaning (e.g. "Posterior-Anterior" and "PA"). For application as the oversight AI model, the detection performances were evaluated for the patient-report misregistration and right-left orientation errors, respectively, as the binary classification problem. The pre-trained model was directly used for evaluation in a zero-shot manner without any fine-tuning. The evaluation was done in the test dataset the same as the retrieval task, by randomly substituting the word "right" was changed to "left" and vice versa with a probability of 5%, and substituting the original report with an unmatched report with a probability of 1% emulating the orientation error and the misregistration error, respectively. A higher probability was adopted for the orientation error, considering that the orientation error is more likely to occur in the clinic compared with the misregistration. The error detection performance was evaluated with the area under the receiver operating characteristics curve (AUC). For evaluation of the oversight AI model's ability to automatically correct the wrong word with the correct one, we masked each word within the sentence one by one and let the model predict the masked word, referring to the corresponding image and unmasked words, as it may predict the word suitable for the image and text contexts if it correctly learned both visual and textual concepts and their semantic correspondences. For classification, the AUC was used as the principal evaluation metric to compare the performances between the models, and the accuracy, precision, and recall were separately reported. For the evaluation of the clinical accuracy of the generated reports for the abdominal radiographs, whether the clinically important abnormal findings (e.g. ileus, pneumoperitoneum) are mentioned in the generated report or not was evaluated. All experiments were repeatedly performed with three different random seeds to validate the reproducibility, and the mean and standard deviation are reported.

Ethic committee approval. The abdominal radiograph data collected for this study were ethically approved by the Institutional Review Boards of Chung-Ang University Hospital, Chungnam University Hospital, Kyungpook National University Hospital, and Yeungnam University Hospital, and the requirement for informed consent was waived.

Reporting Summary

Further information on research design is available in the Nature Research Reporting Summary linked to this article.

Data Availability

Part of the data is collected from open-sourced data repositories that are publicly available. The MIMIC-CXR database is available at <https://physionet.org/content/mimic-cxr/2.0.0/>. The VQA-RAD database is available at <https://osf.io/89kps/>. The preprocessed versions of the MIMIC-CXR and VQA-RAD databases are available at <https://github.com/SuperSupermoon/MedViLL>. The BIMCV data can be found at <https://github.com/BIMCV-CSUSP/BIMCV-COVID-19>. The normal NIH database is available at <https://cloud.google.com/healthcare-api/docs/resources/public-datasets/nih-chest>. Other parts of data that are used for the external validation of COVID-19 classification and the experiments for abdominal radiographs are not publicly available due to the patient privacy obligation. Interested users can request access to these data for research purposes, by contacting the corresponding author J.C.Y (jong.ye@kaist.ac.kr). The data can be shared after the IRB approval and de-identification along with the signed agreement on data transfer and usage. Replies to the initial request will be made within 10 working days. The use of data is limited only to research purposes, and redistribution is prohibited.

Code Availability

The code is available at the following GitHub repository: https://github.com/sangjoon-park/Medical_X-VL.

References

1. Boden, M. A. *Mind as machine: A history of cognitive science* (Oxford University Press, 2008).
2. Jia, C. et al. Scaling up visual and vision-language representation learning with noisy text supervision. In International Conference on Machine Learning, 4904–4916 (PMLR, 2021).
3. Li, J. et al. Align before fuse: Vision and language representation learning with momentum distillation. *Advances in neural information processing systems* **34**, 9694–9705 (2021).
4. Cho, J., Lei, J., Tan, H. & Bansal, M. Unifying vision-and-language tasks via text generation. In International Conference on Machine Learning, 1931–1942 (PMLR, 2021).
5. Chen, Y.-C. et al. Uniter: Universal image-text representation learning. In European conference on computer vision, 104–120 (Springer, 2020).
6. Lu, J., Batra, D., Parikh, D. & Lee, S. Vilbert: Pretraining task-agnostic visiolinguistic representations for vision-and-language tasks. *Advances in neural information processing systems* **32** (2019).
7. Li, X. et al. Oscar: Object-semantics aligned pre-training for vision-language tasks. In European Conference on Computer Vision, 121–137 (Springer, 2020).
8. Huang, Z., Zeng, Z., Liu, B., Fu, D. & Fu, J. Pixel-bert: Aligning image pixels with text by deep multi-modal transformers. *arXiv preprint arXiv:2004.00849* (2020).
9. Dosovitskiy, A. et al. An image is worth 16x16 words: Transformers for image recognition at scale. *arXiv preprint arXiv:2010.11929* (2020).
10. Vaswani, A. et al. Attention is all you need. *Advances in neural information processing systems* **30** (2017).
11. Radford, A. et al. Learning transferable visual models from natural language supervision. In International Conference on Machine Learning, 8748–8763 (PMLR, 2021).
12. Yu, J. et al. Coca: Contrastive captioners are image-text foundation models. *arXiv preprint arXiv:2205.01917* (2022).
13. Wang, W., Bao, H., Dong, L. & Wei, F. Vlmo: Unified vision-language pre-training with mixture-of-modality- experts. *arXiv preprint arXiv:2111.02358* (2021).
14. Alayrac, J.-B. et al. Flamingo: a visual language model for few-shot learning. *arXiv preprint arXiv:2204.14198* (2022).
15. Moon, J. H., Lee, H., Shin, W. & Choi, E. Multi-modal understanding and generation for medical images and text via vision-language pre-training. *arXiv preprint arXiv:2105.11333* (2021).
16. Yan, B. & Pei, M. Clinical-bert: Vision-language pre-training for radiograph diagnosis and reports generation (2022).
17. Lin, T.-Y. et al. Microsoft coco: Common objects in context. In European conference on computer vision, 740–755 (Springer, 2014).
18. Johnson, A. E. et al. Mimic-cxr, a de-identified publicly available database of chest radiographs with free-text reports. *Scientific data* **6**, 1–8 (2019).
19. Xiang, T. et al. In-painting radiography images for unsupervised anomaly detection. *arXiv preprint arXiv:2111.13495* (2021).
20. Chen, F. et al. Vlp: A survey on vision-language pre-training. *arXiv preprint arXiv:2202.09061* (2022).
21. Li, L. H., Yatskar, M., Yin, D., Hsieh, C.-J. & Chang, K.-W. Visualbert: A simple and performant baseline for vision and language. *arXiv preprint arXiv:1908.03557* (2019).
22. Yang, J. et al. Vision-language pre-training with triple contrastive learning. In Proceedings of the IEEE/CVF Conference on Computer Vision and Pattern Recognition, 15671–15680 (2022).

23. Cheng, R., Wu, B., Zhang, P., Vajda, P. & Gonzalez, J. E. Data-efficient language-supervised zero-shot learning with self-distillation. In Proceedings of the IEEE/CVF Conference on Computer Vision and Pattern Recognition, 3119–3124 (2021).
24. Kim, G. Recent deep semi-supervised learning approaches and related works. arXiv preprint arXiv:2106.11528 (2021).
25. Robinson, J., Chuang, C.-Y., Sra, S. & Jegelka, S. Contrastive learning with hard negative samples. arXiv preprint arXiv:2010.04592 (2020).
26. Lowe, H. J. & Barnett, G. O. Understanding and using the medical subject headings (mesh) vocabulary to perform literature searches. *Jama* **271**, 1103–1108 (1994).
27. Lau, J. J., Gayen, S., Ben Abacha, A. & Demner-Fushman, D. A dataset of clinically generated visual questions and answers about radiology images. *Scientific data* **5**, 1–10 (2018).
28. Yu, L. et al. Mattnet: Modular attention network for referring expression comprehension. In Proceedings of the IEEE Conference on Computer Vision and Pattern Recognition, 1307–1315 (2018).
29. Nguyen, B. D. et al. Overcoming data limitation in medical visual question answering. In International Conference on Medical Image Computing and Computer-Assisted Intervention, 522–530 (Springer, 2019).
30. Eslami, S., de Melo, G. & Meinel, C. Does clip benefit visual question answering in the medical domain as much as it does in the general domain? arXiv preprint arXiv:2112.13906 (2021).
31. Papineni, K., Roukos, S., Ward, T. & Zhu, W.-J. Bleu: a method for automatic evaluation of machine translation. In Proceedings of the 40th annual meeting of the Association for Computational Linguistics, 311–318 (2002).
32. Lin, C.-Y. Rouge: A package for automatic evaluation of summaries. In Text summarization branches out, 74–81 (2004).
33. Banerjee, S. & Lavie, A. Meteor: An automatic metric for mt evaluation with improved correlation with human judgments. In Proceedings of the acl workshop on intrinsic and extrinsic evaluation measures for machine translation and/or summarization, 65–72 (2005).
34. Vedantam, R., Lawrence Zitnick, C. & Parikh, D. Cider: Consensus-based image description evaluation. In Proceedings of the IEEE conference on computer vision and pattern recognition, 4566–4575 (2015).
35. Irvin, J. et al. Chexpert: A large chest radiograph dataset with uncertainty labels and expert comparison. In Proceedings of the AAAI conference on artificial intelligence, vol. 33, 590–597 (2019).
36. Selvaraju, R. R. et al. Grad-cam: Visual explanations from deep networks via gradient-based localization. In Proceedings of the IEEE international conference on computer vision, 618–626 (2017).
37. Chen, T., Kornblith, S., Norouzi, M. & Hinton, G. A simple framework for contrastive learning of visual representations. In International conference on machine learning, 1597–1607 (PMLR, 2020).
38. Caron, M. et al. Emerging properties in self-supervised vision transformers. In Proceedings of the IEEE/CVF International Conference on Computer Vision, 9650–9660 (2021).
39. Xie, Z. et al. Simmim: A simple framework for masked image modeling. In Proceedings of the IEEE/CVF Conference on Computer Vision and Pattern Recognition, 9653–9663 (2022).
40. Yang, J. et al. Unified contrastive learning in image-text-label space. In Proceedings of the IEEE/CVF Conference on Computer Vision and Pattern Recognition, 19163–19173 (2022).
41. Wang, Z. et al. Simvlm: Simple visual language model pretraining with weak supervision. arXiv preprint arXiv:2108.10904 (2021).
42. Dou, Z.-Y. et al. Coarse-to-fine vision-language pre-training with fusion in the backbone. arXiv preprint arXiv:2206.07643 (2022).
43. He, K., Fan, H., Wu, Y., Xie, S. & Girshick, R. Momentum contrast for unsupervised visual representation

learning. In Proceedings of the IEEE/CVF conference on computer vision and pattern recognition, 9729–9738 (2020).

44. Devlin, J., Chang, M.-W., Lee, K. & Toutanova, K. Bert: Pre-training of deep bidirectional transformers for language understanding. arXiv preprint arXiv:1810.04805 (2018).
45. Zhou, J. et al. ibot: Image bert pre-training with online tokenizer. arXiv preprint arXiv:2111.07832 (2021).
46. Bao, H., Dong, L. & Wei, F. Beit: Bert pre-training of image transformers. arXiv preprint arXiv:2106.08254 (2021).
47. Signoroni, A. et al. Bs-net: Learning covid-19 pneumonia severity on a large chest x-ray dataset. *Medical Image Analysis* **71**, 102046 (2021).
48. Wang, X. et al. Chestx-ray8: Hospital-scale chest x-ray database and benchmarks on weakly-supervised classification and localization of common thorax diseases. In Proceedings of the IEEE conference on computer vision and pattern recognition, 2097–2106 (2017).

Correspondence

Correspondence and requests for materials should be addressed to Jong Chul Ye. (email: jong.ye@kaist.ac.kr).

Acknowledgments

This research was supported by the KAIST Key Research Institute (Interdisciplinary Research Group) Project, the National Research Foundation of Korea under Grant NRF-2020R1A2B5B03001980, and Chungnam National University Hospital Research Fund, 2022.

Author Contributions

S.P. performed all experiments, wrote the extended code, and prepared the manuscript. E.S.L and J.E.L collected data and provided clinical evaluations. J.C.Y. supervised the project in conception and discussion and prepared the manuscript.

Competing Interests

The authors declare that they have no competing financial interests.

Supplementary Information

Supplementary Table 1: Ablation study of the key components for medical X-VL model.

Method	Image-to-report			Report-to-image		
	R@1	R@5	R@10	R@1	R@5	R@10
w/o Alternating fusion encoder	59.0 (0.4)	88.4 (0.6)	95.0 (0.4)	60.0 (0.4)	88.7 (0.3)	94.7 (0.2)
w/o Ensemble (text only)	60.6 (1.4)	89.6 (0.3)	95.5 (0.2)	63.2 (0.5)	90.4 (0.4)	95.0 (0.2)
w/o Ensemble (vision only)	59.1 (1.2)	89.0 (0.2)	95.5 (0.2)	61.2 (0.2)	89.7 (0.2)	95.0 (0.2)
w/o Contrastive learning	7.7 (0.9)	15.6 (1.0)	23.2 (0.8)	6.3 (1.1)	14.3 (1.3)	22.2 (1.1)
w/o Masked language modeling	50.8 (0.9)	83.3 (0.5)	92.5 (0.4)	52.0 (1.5)	84.7 (0.5)	92.1 (0.2)
w/o Masked image modeling	58.9 (0.4)	87.8 (0.7)	94.3 (0.2)	60.3 (0.7)	88.6 (0.3)	94.0 (0.0)
w/o Knowledge distillation	46.4 (0.9)	80.0 (0.6)	89.8 (0.6)	47.6 (0.3)	81.1 (0.2)	89.1 (0.0)
w/o Hard negative mining	58.0 (1.4)	88.8 (0.3)	95.0 (0.3)	58.3 (1.3)	89.0 (0.4)	94.4 (0.2)
w/o Medical keyword weighting	60.7 (1.1)	89.1 (0.7)	95.2 (0.2)	62.5 (0.4)	89.6 (0.2)	94.7 (0.6)
Proposed	61.3 (1.4)	89.8 (0.2)	95.5 (0.2)	63.2 (0.2)	90.5 (0.3)	95.0 (0.2)

All experiments are performed with three different random seeds, and the means (standard deviations) are provided.

Supplementary Table 2: Detailed hyperparameters for the vision-language pre-training and downstream tasks.

Hyperparameters	Pre-training	Report generation	VQA	Classification
Batch size	12	12	32	64
Optimizer	AdamW	AdamW	AdamW	AdamW
Scheduler	Warmup cosine	Warmup cosine	Warmup cosine	Warmup cosine
Learning rate (min)	0.00001	0.00001	0.00001	0.000001
Learning rate (max)	0.0001	0.0001	0.0001	0.00001
Epoch (total)	15	15	50	30
Epoch (warm-up)	5	5	10	10
Patch masking ratio	0.3	0.3	-	-
Word masking ratio	0.15	-	-	-
λ for distillation	0.4	0.4	-	-

VQA, vision question answering.

Supplementary Table 3: Detailed hyperparameters for other self-supervised learning methods.

Hyperparameters	SimCLR ¹	DINO ²	SimMIM ³
Batch size	32	32	128
Optimizer	Adam	AdamW	AdamW
Scheduler	Cosine annealing	Warmup cosine	Warmup multistep
Learning rate (min)	-	0.000001	0.0000005
Learning rate (max)	0.00005	0.00005	0.0001
Epoch (total)	15	10	100
Epoch (warm-up)	-	1	20
Patch masking ratio	-	-	0.6

VQA, vision question answering.

A



The boys are playing on the ground.

↕
"children"
"kids"

↕
"field"
"grass"

Large
differences
↔



A bus is parked alongside the road.

B



No pneumonia or pneumothorax is observed.

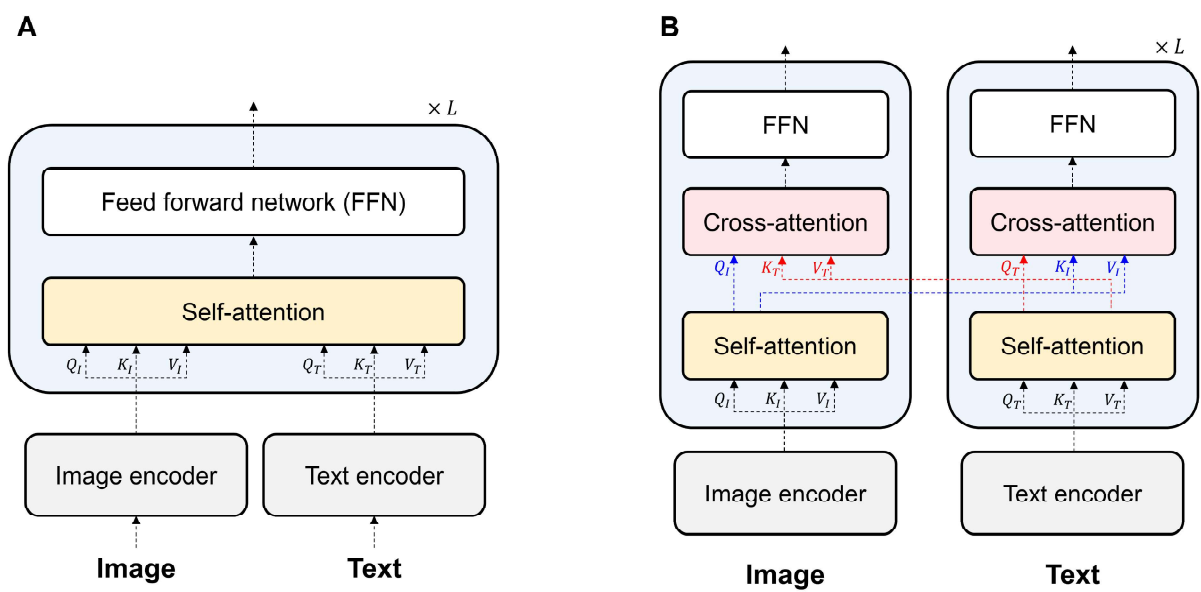
↕
Unique and hard to be substituted

Small
differences
↔

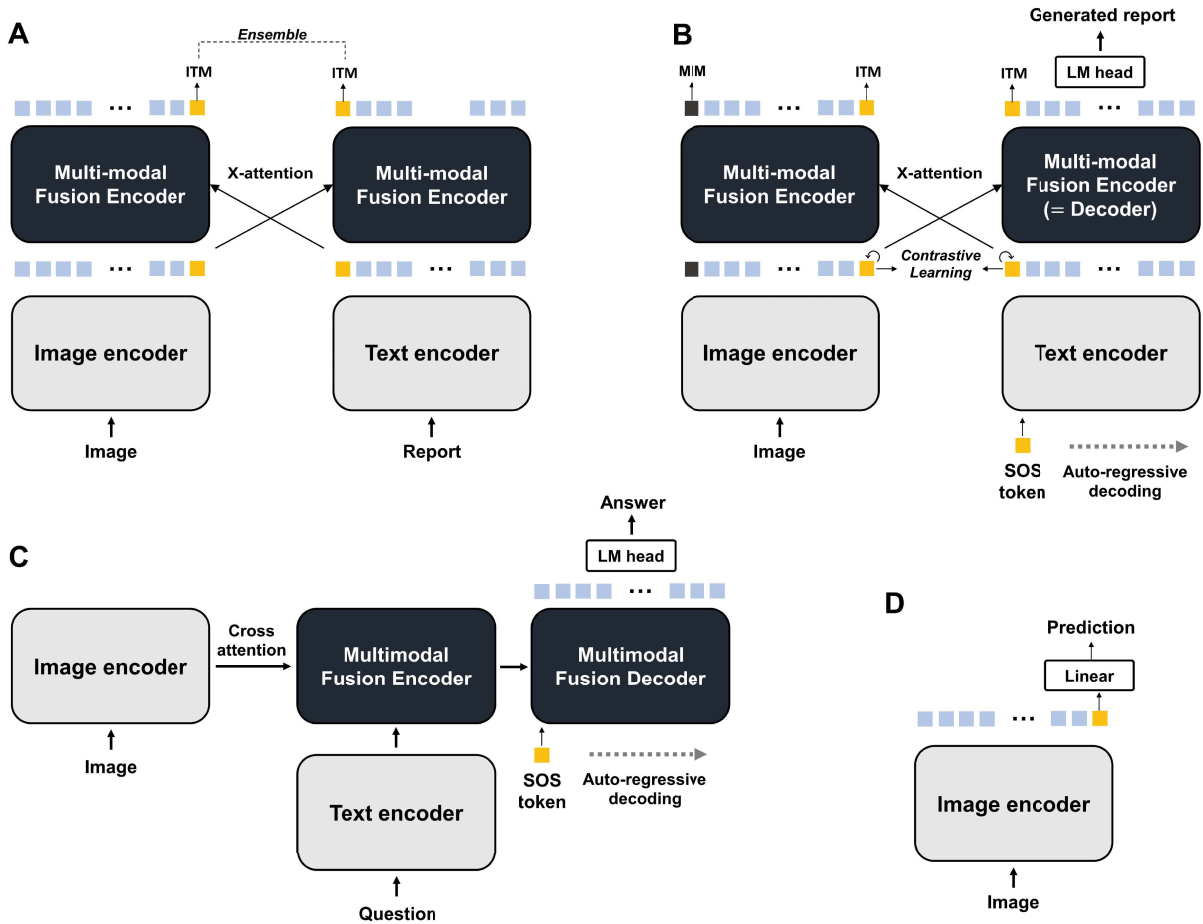


Mild lung opacities are observed in the right lower lobe.

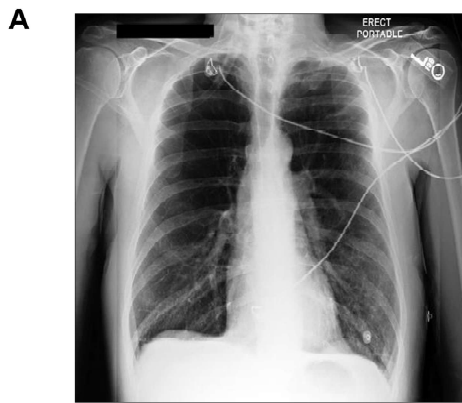
Supplementary Fig. S1: Differences between data in computer vision and medical domain. (A) For the photographic images, the different samples consist of totally different semantic components. In addition, the important words in the caption can be substituted with other words with the same meaning. (B) For the medical images, the differences between the samples are subtle, albeit describing different findings. In the medical reports, some keywords are unique and can hardly be substituted. The examples are from the MS-COCO⁴ and MIMIC-CXR⁵ datasets.



Supplementary Fig. S2: Illustration of the different vision-language model architectures. (A) The single stream architecture receives the features from the image and text encoders, and processes them with a single multi-modal transformer encoder equipped with self-attention. Meanwhile, (B) the dual-stream architecture processes the image and text features separately, with the explicit cross-modal attention between two modalities as well as the intra-modal self-attention.



Supplementary Fig. S3: Adaptation of the medical X-VL model for downstream tasks. (A) For zero-shot retrieval, the ensemble of prediction from image-to-text and text-to-image pathways is used. (B) For report generation, the multi-modal encoder is used as an auto-regressive decoder to generate text instead of masked language modeling (MLM), with other learning objectives remaining the same as in pre-training. (C) Similarly, the vision question answering problem was solved as an answer-generating task. (D) For classification, a pre-trained image encoder was used as the backbone for the classification model. ITM, image-text matching; MIM, masked image modeling; LM, language modeling; SOS, start of a sequence.



↓ Medical X-VL

Correct report: The lungs are hyperinflated but clear of consolidation. The cardiomeastinal silhouette is within normal limits. osseous structures are unremarkable. Single portable view of the chest.

1st matching: The lungs are hyperinflated but clear of consolidation. The cardiomeastinal silhouette is within normal limits. osseous structures are unremarkable. Single portable view of the chest.

2nd matching: There is mild hyperexpansion of the lungs suggesting some underlying chronic pulmonary disease. No previous images. Of incidental note is an old healed rib fracture on the right. However no evidence of acute pneumonia vascular congestion or pleural effusion.

⋮

Worst matching: Extensive consolidation in the left lower lobe and accompanying small-to-moderate pleural effusion have varied in size no larger today than on _____. AP chest compared to _____. Nasogastric tube ends in the upper stomach. Transvenous right atrial and right ventricular pacer leads are unchanged in their respective positions. Right pic line can be traced as far as the junction of the right subclavian and jugular veins. Mild-to-moderate cardiomegaly and a generally enlarged thoracic aorta are also stable. Borderline edema persists in the right lung. No pneumothorax.

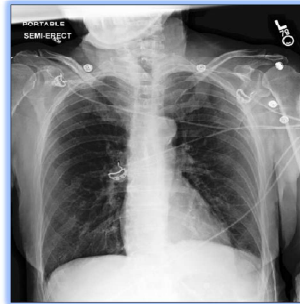
B The lungs are hyperinflated but clear of consolidation. The cardiomeastinal silhouette is within normal limits. osseous structures are unremarkable. Single portable view of the chest.

↓ Medical X-VL

1st matching



2nd matching

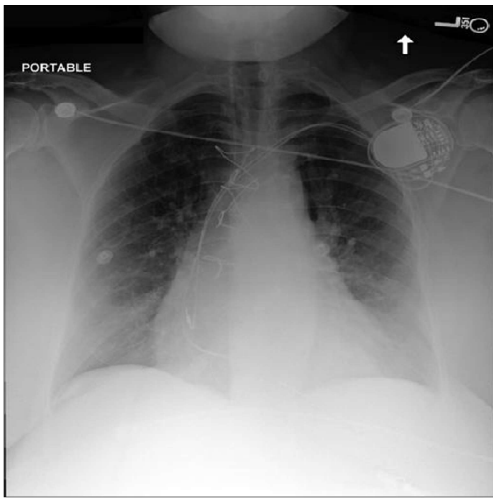


⋮

Worst matching

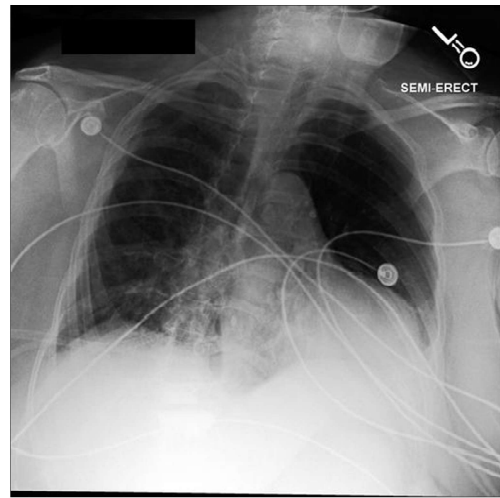


Supplementary Fig. S4: Examples of image-to-text and text-to-image retrievals. (A) In image-to-text retrieval, the model correctly matched the ground truth report corresponding to the given image and retrieved the other image with a similar semantic meaning the second. A report with totally different findings is considered the worst matching one. (B) In text-to-image retrieval, the model correctly retrieved the image corresponding to the given report, and the second-best matching image retrieved by the model also shows almost the same findings (e.g. hyperinflation of the lung with no clear abnormality). On the contrary, the worst matching image considered by the model shows completely different findings (e.g. multiple opacities more severe for the left lower lobe than the right).

A

Label: The patient is status **post median sternotomy**. Left-sided pacer device is seen with leads extending to the expected positions of the **right atrium and right ventricle**. The **cardiac silhouette is mildly enlarged**. Mediastinal contours are unremarkable. There may be **minimal central vascular engorgement** without overt pulmonary edema. No large pleural effusion is seen. There is no evidence of pneumothorax or focal consolidation. The lungs appear relatively hyperinflated.

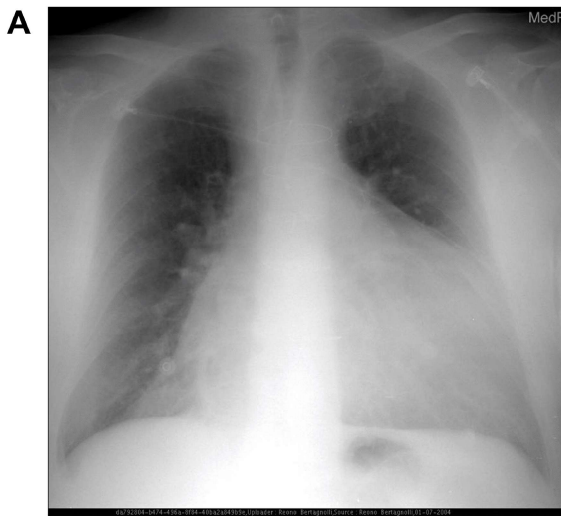
Generated: Patient is status **post median sternotomy** CABG and left-sided dual-chamber pacemaker device with leads terminating in the **right atrium and right ventricle**. **Mild cardiomegaly** is unchanged. Mediastinal and hilar contours are similar. There is **mild pulmonary vascular congestion**. No focal consolidation pleural effusion or pneumothorax is present. No acute osseous abnormalities detected.

B

Label: In comparison with the study of ___ the patient is somewhat oblique limiting the evaluation. However there is no evidence of pneumothorax. overall probably **little change**.

Generated: In comparison with the study of ___ there is **little overall change**. Obliquity of the patient makes it difficult to evaluate the heart and lungs. However there is no evidence of acute pneumonia or vascular congestion.

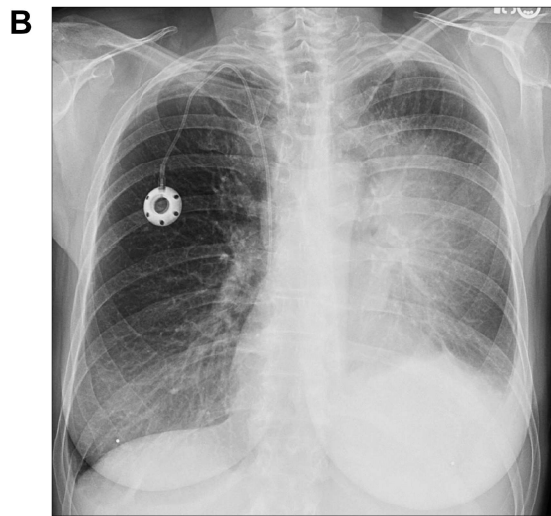
Supplementary Fig. S5: Examples of the generated reports for chest radiographs. (A) For the chest radiograph, the model successfully mentioned important semantics (colored text), albeit different in detailed expressions. (B) In addition, it can identify the inadequacy of the image quality due to the problem of patient position during image acquisition.



Question: What is the pathology?

Label answer: Cardiomegaly with pulmonary edema

Predicted answer: Cardiomegaly with pulmonary edema

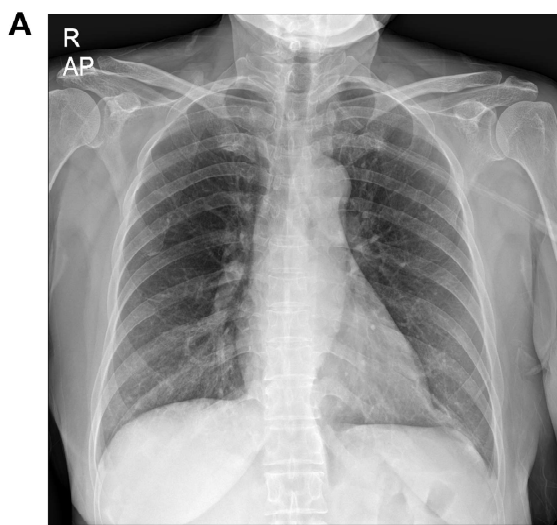


Question: Is the left lung field more radioopaque than the right side?

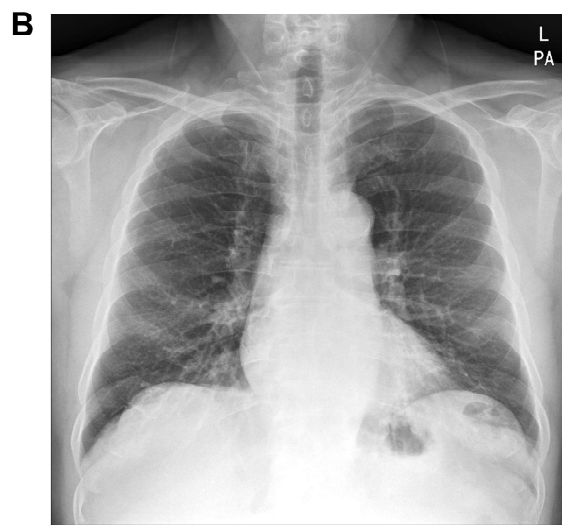
Label answer: Yes

Predicted answer: Yes

Supplementary Fig. S6: Examples of the vision-question answering. (A) For the open-ended question, the model correctly answered the multiple pathologies of the given image. (B) For the closed-ended question, the model correctly answered relative radioopacities in consideration of the lesion location and right-left orientation.



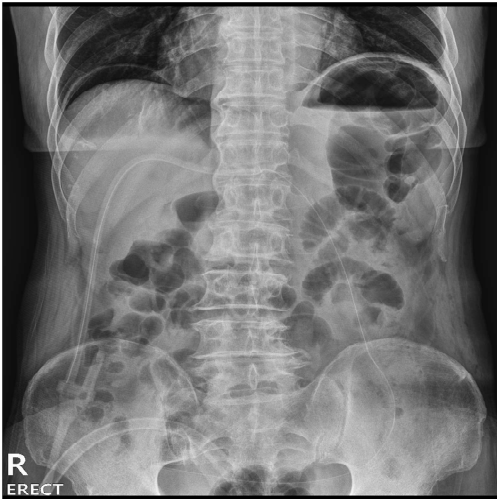
Label: COVID-19 → **X-VL: COVID-19**
SimCLR: Normal
DINO: Normal
SimMIM: Normal



Label: Normal → **X-VL: Normal**
SimCLR: COVID-19
DINO: COVID-19
SimMIM: COVID-19

Supplementary Fig. S7: Examples of the classification with limited data for newly emerging diseases. Compared with the models pre-trained with other self-supervised learning methods, the vision-language pre-trained model with the proposed X-VL provided correct predictions for both (A) mild COVID-19 positive and (B) negative cases without confusion.

A



Label: Mild post-op. ileus and a small amount of pneumoperitoneum.

Generated: Mild post-op. ileus and a small amount of pneumoperitoneum.

B



Label: Non specific bowel gas pattern.

Generated: Non specific bowel gas pattern.

Supplementary Fig. S8: Examples of the generated reports for abdomen radiographs. For the abdomen radiograph, the model correctly generated a report describing (A) the pathologic findings as well as the (B) normal condition.

References

1. Chen, T., Kornblith, S., Norouzi, M. & Hinton, G. A simple framework for contrastive learning of visual representations. In *International conference on machine learning*, 1597–1607 (PMLR, 2020).
2. Caron, M. *et al.* Emerging properties in self-supervised vision transformers. In *Proceedings of the IEEE/CVF International Conference on Computer Vision*, 9650–9660 (2021).
3. Xie, Z. *et al.* Simmim: A simple framework for masked image modeling. In *Proceedings of the IEEE/CVF Conference on Computer Vision and Pattern Recognition*, 9653–9663 (2022).
4. Lin, T.-Y. *et al.* Microsoft coco: Common objects in context. In *European conference on computer vision*, 740–755 (Springer, 2014).
5. Johnson, A. E. *et al.* Mimic-cxr, a de-identified publicly available database of chest radiographs with free-text reports. *Scientific data* **6**, 1–8 (2019).